Characterization of the acoustic output of single marine-seismic airguns and clusters: The Svein Vaage dataset

Mark K. Prior,[1,a)] Michael A. Ainslie,[2,b)] Michele B. Halvorsen,[3,c)] Iris Hartstra,[1,d)] Robert M. Laws,[4,e)] Alexander MacGillivray,[5,f)] Roel Müller,[1,g)] Stephen Robinson,[6,h)] and Liansheng Wang[6]

[1]*Acoustics and Sonar Department, TNO, Oude Waalsdorperweg 63, Den Haag, 2597 AK, The Netherlands*

[2]*JASCO Applied Sciences (Deutschland) GmbH, Mergenthaler Allee 15-21, Eschborn, Hesse, 65760, Germany*

[3]*Jackson Estuarine Laboratory, College of Life Sciences and Agriculture, University of New Hampshire, 85 Adams Point Road, Durham, New Hampshire 03824, USA*

[4]*Havakustik Ltd., Cliftonville, George Street, Cambridge, CB4 1AJ, United Kingdom*

[5]*JASCO Applied Sciences (Canada), Victoria, British Columbia V8Z 7X8, Canada*

[6]*National Physical Laboratory, Hampton Road, Teddington, TW11 0LW, United Kingdom*

ABSTRACT:

The acoustical output of marine-seismic airguns is determined from recordings of the sound pressure made on hydrophones suspended below a floating barge from which the airguns are also deployed. The signals from multiple types of airguns are considered and each type is operated over a range of deployment depths and chamber pressures. The acoustical output is characterized in terms of a "source waveform" with dimensions of the pressure-times-distance and in an infinite idealized medium, could be divided by the source-receiver distance to give the sound pressure at that receiver. In more realistic environments, the source waveform may be used to predict the pressure at any arbitrary receiver position simply by the application of a time-domain transfer function describing the propagation between the source and receiver. The sources are further characterized by metrics such as the peak source waveform and energy source level. These metrics are calculated in several frequency bands so that the resulting metrics can be used to characterize the acoustical output of the airguns in terms of their utility for seismic image-processing or possible effects on marine life. These characterizations provide reference data for the calibration of models that predict the airguns' acoustical output. They are validated via comparisons of the acoustic pressure measured on far-field hydrophones and predicted using the source waveforms. Comparisons are also made between empirically derived expressions relating the acoustic metrics to the chamber volume, chamber pressure, and deployment depth and similar expressions from the literature. © *2021 Acoustical Society of America.* https://doi.org/10.1121/10.0006751

(Received 11 June 2021; revised 8 September 2021; accepted 29 September 2021; published online 16 November 2021)

[Editor: Nicholas P. Chotiros]   Pages: 3675–3692

I. INTRODUCTION

Subsea oil and gas reserves are mapped and monitored by geophysical surveys (widely known as "seismic surveys"), which use impulsive sound generated by the rapid release of compressed air. The compressed-air sources of this impulsive sound are widely known as "airguns"; see, for example, Ewing and Zaunere (1964), Ziolkowski *et al.* (1982), and Giles and Johnston (1973).

Airguns generate high-amplitude, low-frequency, impulsive signals that are designed to allow echoes to be detected from sub-seabed geological structures, including those that might indicate the presence of oil or gas (Dragoset, 2000; IAGC, 2011). To increase the signal amplitude, reduce "bubble pulses," and increase the spectral flatness, airguns are typically deployed in arrays made up of multiple devices of different sizes and, therefore, different resonant frequencies. All of the airguns in an array are usually operated at the same chamber pressure and often all are deployed in a horizontal plane at a depth in the range of 5–15 m.

The acoustic signals emitted by the airguns have several distinct features. An example is shown in Fig. 1. In the time domain, they are characterized by an early, rapid rise in the sound pressure, associated with the initial release of air. This is followed by a less rapid drop in the pressure, and this reduction continues until the sound pressure is negative. This portion of the signal is associated with the motion of the bubble formed by the released air. This bubble initially expands and "overshoots" as a result of the momentum of the expansion, causing the pressure in the bubble to be less

[a)]Electronic mail: mark.prior@tno.nl, ORCID: 0000-0002-1421-1429.
[b)]ORCID: 0000-0002-0565-3559.
[c)]Also at: School of Marine Science and Ocean Engineering, University of New Hampshire, 85 Adams Point Road, Durham, NH 03824, USA. ORCID: 0000-0002-2495-7574.
[d)]ORCID: 0000-0002-9266-4706.
[e)]ORCID: 0000-0001-6640-4022.
[f)]ORCID: 0000-0003-2778-2017.
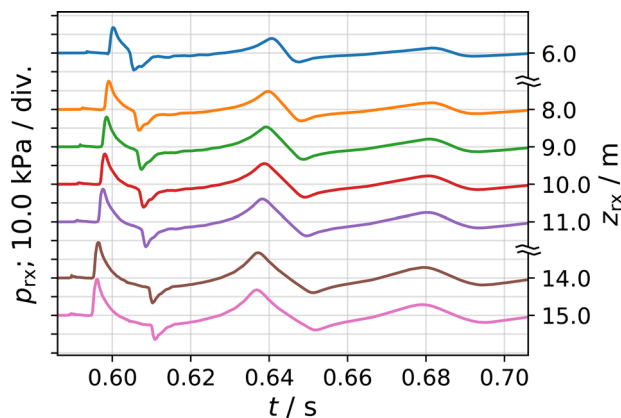[g)]ORCID: 0000-0002-5055-5544.
[h)]ORCID: 0000-0003-1497-9371.

FIG. 1. (Color online) The pressure signals from an airgun emission at 20 m depth were recorded by an array of hydrophones at 14.6 m horizontal distance (see Fig. 2). The signals corresponding to the malfunctioning hydrophones are discarded, which is indicated by the broken axis on the right. The primary peak travels up along the array shortly before 0.60 s, decreasing in amplitude because of the spherical spreading of the sound wave. The surface reflection of this primary peak travels back down the array around 0.61 s, again, decreasing because of spherical spreading. After the maximum expansion of the bubble, recorded around 0.62 s, the bubble collapses, leading to the second peak and surface reflections around 0.64 s. This process continues with a decreasing amplitude resulting from the energy loss by the radiation. One more peak with reflection is shown around 0.69 s. The data shown for the gun type: Bolt 1500, volume, 80 in^3 (1.3 dm^3); depth, 20.0 m; chamber pressure, 2000 lbf in.$^{-2}$ (13.79 MPa).

than the surrounding hydrostatic pressure. The bubble subsequently contracts, collapses, and rebounds from a minimum volume to expand again. The collapse of the bubble is associated with a second, positive peak of the acoustic pressure. The bubble oscillation may continue for several cycles of expansion and contraction with the airgun's acoustical output showing repeated positive peaks. These features are contained in the "source waveform" (ISO, 2017), which is the fundamental description of the airgun's acoustical output in the form of a time-series of pressure-distance values which, when combined with a propagation transfer function between the source and receiver, gives the pressure at the receiver.

At-sea recordings of the acoustic pressure emitted by the airguns show a negated image of the initial peak. This image is caused by a reflection at the sea surface and arrives at the receiver with the same time and amplitude as if there were a negated "image airgun" placed above the sea surface at a height equal to the deployment depth of the actual airgun. This "surface ghost" is also present for subsequent peaks of the emitted pressure and a characteristic feature of the surface-affected source waveform (ISO, 2017) of the airgun and its surface-reflected image. In the frequency domain, the source spectrum (ISO, 2017) of the airguns' acoustical output shows that the bulk of the emitted power is concentrated at frequencies below a few hundred hertz. These are the frequencies best suited for geophysical exploration and in this frequency band, the signals emitted by the airguns show high repeatability between emissions. At higher frequencies, the emitted power drops sharply and the sound-generation processes become stochastic, showing

poor repeatability between emissions (MacGillivray, 2019). Although the proportion of the airguns' total power emitted at these frequencies is small, the signals may still be detectable above the background noise levels at these frequencies several kilometers away from the airgun. This long-range detectability decreases at very high frequencies because of absorption of the sound in the body of the water.

There is increasing scientific and societal interest in the risk of the impact of the sound generated by airguns during marine-seismic surveys on marine life (Stone and Tasker 2006; McCauley et al., 2017; Fields et al., 2019; Slabbekoorn et al., 2019). This has resulted in the formulation of regulations and guidelines (Southall et al., 2019; NMFS, 2018; Dekeling et al., 2014), and the mitigation of this risk for airguns is an active field of research (Coste et al., 2014). This concern has also motivated research into sound sources, which might provide an alternative to arrays of airguns (Pramik, 2013; Duncan et al., 2017). The potential impact on aquatic life of the sound emitted by airguns extends to frequencies higher than those usually used in marine-seismic imaging. Although airguns concentrate their emissions at frequencies below approximately 150 Hz, they also emit sound at higher frequencies. This high-frequency sound, although representing a small proportion of the airguns' total acoustic output, may remain above the background noise levels that are kilometers from the airgun arrays. This means that any full assessment of the environmental impact of the airguns' acoustical emissions must extend to frequencies above those normally considered by the marine-seismic community.

Fundamental to any objective analysis of this topic is an understanding of the properties of airguns as sound sources, both individually and when deployed in arrays (Laws et al., 1990; Duncan and Gavrilov, 2019; MacGillivray, 2006; Sertlek and Ainslie, 2015; Goertz et al., 2013). Significant uncertainty remains in the prediction of the acoustic output of airguns, particularly at frequencies higher than those typically used in seismic imaging (around 150 Hz) but which may be important for calculation of the environmental impact (Ainslie et al., 2019; Ainslie et al., 2016). This uncertainty arises from the prediction of different levels of sound radiation, which is made by various prediction methods. Validation of airgun source models via comparison between the predicted and measured acoustic output is an important step in the reduction of this uncertainty.

Systematic measurements of sound emitted from single airguns and airgun clusters were commissioned by the E and P Sound and Marine Life Joint Industry Programme (E&P Sound and Marine Life Joint Industry Programme, London, UK) and performed by Petroleum Geo-Services (PGS; Lilleaker, Norway) in 2007 and 2009–2010 using equipment suspended from barges in Hjørunfjord and Storfjorden, Norway (Lundsten, 2010). This experiment was named the "Svein Vaage Broadband Air Gun Study" in honor of the late geophysicist's contribution to the field of marine seismic surveying (Mattsson et al., 2012). The dataset resulting from this study, referred to henceforth as the "Svein Vaage

(SV) data," is suitable for the characterization of the acoustical properties of individual airguns and airgun clusters.

For each airgun type, measurements were made for several different combinations of the chamber pressure, operating depth, and chamber volume. The effects of the varying separation of the individual airguns within the clusters were also measured. For each combination, a sequence of around 50 emissions (also referred to as "discharges" or "shots") was performed, resulting in tens of thousands of signals recorded on each of approximately 20 hydrophones located at a variety of positions. These signals were acquired with sampling frequencies of up to 102.4 kHz, resulting in approximately half a million shot-channel combinations and 660 gigabytes of data.

The SV data were gathered to establish a definitive dataset to characterize the acoustic properties of single airguns and airgun clusters. The data were intended for calibration and validation of airgun-modelling tools, including those capable of producing estimates at frequencies and angles beyond those typically used for seismic imaging.

The sensors deployed include hydrophones and accelerometers. The present analysis focuses attention on the hydrophones as the accelerometers were deployed only during 2010 for a limited subset of the measurements; see (Warner *et al.*, 2018) for a separate analysis and summary of the accelerometer measurements.

The SV dataset contains measurements of the acoustic pressure at fixed locations relative to the airguns. This does not, in itself, represent a characterization of those airguns as acoustic sources. Propagation and geometric effects mean that the pressure signals measured by the receivers vary with the hydrophone position. If a description of the acoustical output of the airgun is sought, such that it is a property only of the source and not of any receiver, then extra processing is required to produce this definitive acoustical characterization.

The purpose of this paper is to characterize airguns and airgun clusters in terms of their source waveforms (ISO, 2017) and corresponding spectra, which are suitably modified to account for airgun-airgun interactions (Ziolkowski *et al.*, 1982). In principle, these can be combined to provide the source waveform for an airgun array (Vaage and Ursin, 1987; Ziolkowski *et al.*, 1982; MacGillivray, 2019), but this is outside our present scope. Alternatively, the sound field computed from the individual airguns can be combined to form the sound field for an array (Heaney and Campbell, 2019; Prior *et al.*, 2019).

In Sec. II, the acoustical terminology used throughout the paper is introduced. The measurement procedure is summarized in Sec. III. Measurements of the sound pressure are described in Sec. IV, and the methodology by which these were used to characterize airguns is set out in Sec. V. Via comparison between the measured and predicted far-field sound pressures at deep receivers, the validation of these characterizations is described in Sec. VI. The utility of the resulting dataset of the source characterizations is discussed and conclusions drawn.

II. TERMS AND DEFINITIONS

Acoustical terminology follows ISO (2017) and the Joint Industry Programme (JIP) terminology standard (Ainslie *et al.*, 2018a). Additional terms and definitions are listed in Table I.

III. SUMMARY OF MEASUREMENTS

The measurement campaign for the SV study was conducted by PGS from a test barge in two different fjords on the Norwegian coast (Fig. 2). The airguns and sensor arrays were suspended from the barge, which was allowed to drift in the current during the measurements. Personnel and other experimental apparatus were likewise situated on the test barge. Daily sound speed measurements were obtained using a time-of-flight sound velocimeter, and daily weather observations were used to log the approximate sea-state and wind conditions.

In total, PGS recorded 61 sequences in 2007 and 332 sequences in 2009–2010, where each sequence corresponds to a collection of repeated emissions of a single airgun (or cluster) on a single day deployed at a specific depth at a specific chamber pressure. The SV data includes measurements for seven different types of airguns: Sercel G-gun, Sercel G-gun II, Sercel GI gun (Sercel, Nantes, France), Bolt 1500

TABLE I. Glossary of terms.

| Term	Definition
Chamber volume	Nominal volume of the space in which the compressed air of an airgun is constrained before it is released into the surrounding water
	Note: For a generator-injector (GI) gun, this is the sum of the nominal volumes of the generator and injector chambers.
Chamber pressure	Difference between the pressure of the compressed air inside the airgun just before it is fired and the atmospheric pressure
Source waveform, synonym: notional source signature	Product of the distance in a specified direction, r, from the acoustic center of a sound source and the delayed far-field sound pressure, $p(t - t_0 + r/c)$, for a specified time origin, t_0, if placed in a hypothetical infinite uniform lossless medium of the same density and sound speed, c, as the actual medium at the location of the source with identical motion of all acoustically active surfaces as the actual source in the actual medium
	Note: The source waveform has the dimensions of the pressure-distance. If combined with a transfer function describing the propagation from the source location to a receiver location, it yields the pressure time-series at the receiver. This is true for any receiver location, including those at long distances from the acoustic source where "spherical spreading: is not a good model of acoustic propagation.
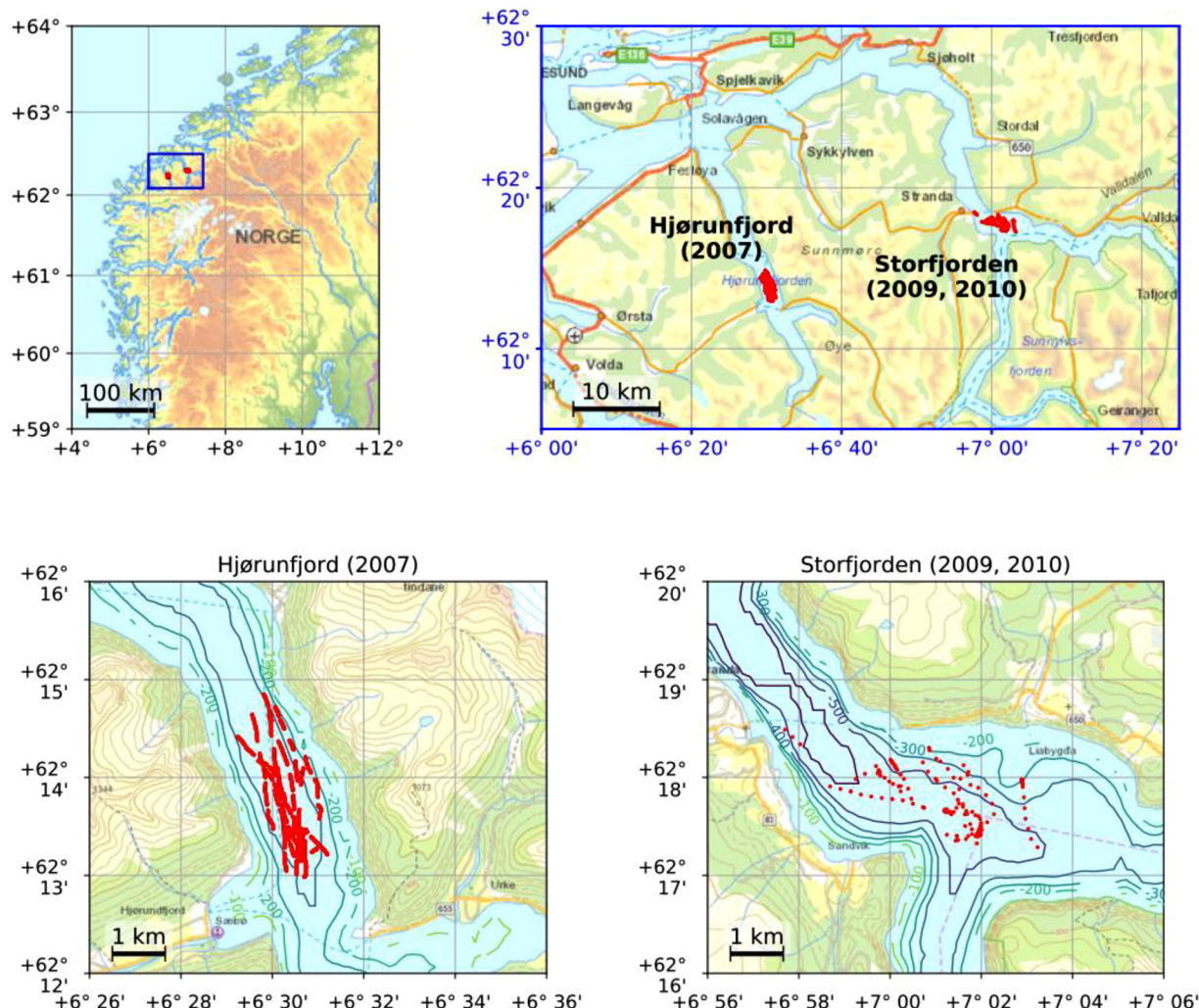
FIG. 2. (Color online) The location of the measurement sites at the Norwegian coast (background, Kartverket, Geovekst og kommuner–Geodata AS).

LL, Bolt 1900 LLXT, Bolt Annular Port Gun (APG), and IO Sleeve Gun (Teledyne Bolt, Houston, TX). The chamber volumes for the single airguns ranged from 10 to 520 in.^{3} (0.16–8.52 liters), and the measured source depths ranged from 1 to 25 m.

Three different types of calibrated hydrophones were used at various distances and elevation angles from the airgun to measure its sound pressure data with low sensitivity hydrophones (AGH 1500C, AG Geophysical, Dallas, TX) at close range (≤ 1.5 m) and higher sensitivity hydrophones (BRÜEL & KJÆR, Nærum, Denmark, and RESON, Slangerup, Denmark) further away (>15 m) in the configuration as shown in Fig. 3. The signals from the hydrophones were passed through a signal conditioner before being digitized by an analog-to-digital converter (ADC). The SV data were stored in SEG-Y (Barry *et al*., 1975) format along with documentation and initial quality assurance (QA)/quality control (QC) information. Additional information regarding the experimental setup and data acquisition particulars are provided in Lundsten (2010).

The quality of the raw data is good in general, but there are some unusable data mainly due to hardware problems.

Screening of the dataset was performed by the authors to identify high-quality data for the intended use. Some sensors were damaged by a storm in 2009 and did not provide data over the full experiment, whereas others suffered from calibration problems throughout. Nevertheless, the SV dataset provides a unique and comprehensive collection of high-quality data that may be used to characterize a broad range of marine-seismic airguns as sources of the underwater sound.

IV. MEASUREMENTS OF SOUND PRESSURE

A systematic review of the SV data found that the Bruel and Kjær, Nærum, Denmark hydrophone channels (i.e., the ones in the corner and center arrays) generally had the best data quality in terms of calibration consistency, frequency response (± 2 dB over the range 3–100 000 Hz) and system self-noise. Furthermore, the absolute calibrations of the BRÜEL & KJÆR, Nærum, Denmark hydrophones were considered the most reliable because their sensitivities were verified during the experiment via pistonphone calibrations at 250 Hz. The sensitivities of the other hydrophone models were verified by cross-calibration against the BRÜEL & KJÆR
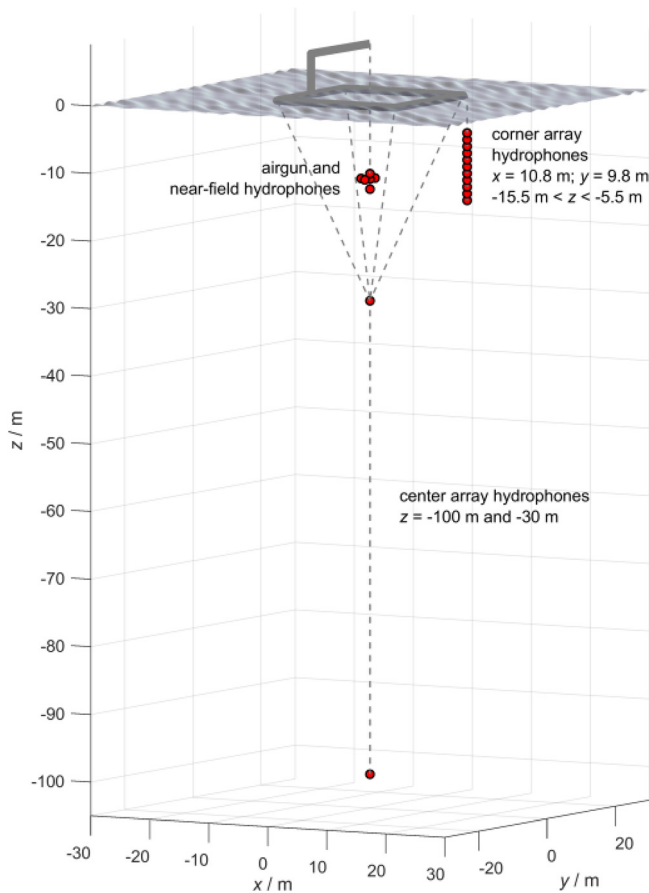
FIG. 3. (Color online) The layout of the hydrophones deployed from the surface barge.

hydrophones (Prior *et al.*, 2018). Thus, to derive the acoustic signature of the airguns over the largest possible signal bandwidth available with the sampling frequency, only the signals from the BRÜEL & KJÆR 8105 hydrophones were used because of the limitations in the frequency response and calibrations of the other two types of hydrophones. Nonetheless, during a manual review, some of the BRÜEL & KJÆR channels were found to be affected by data quality issues such as drop-outs or low-frequency distortion of the airgun signals. Issues with the data quality on the BRÜEL & KJÆR hydrophones were avoided by excluding the affected channels and sequences.

To correct the nominal sound pressure traces in the SEG-Y (Barry *et al.*, 1975) files for artefacts introduced in the recording process and recover, as nearly as possible, the sound pressures generated by the airguns at the time of the measurement, two main preprocessing stages were applied to the data. In the first stage, the hydrophone recordings were compensated for by applying the frequency-dependent instrument response of the hydrophones, which was assumed to be invariant with the depth. A first-order, pole-zero inverse filter (with a passband beginning at 1.3 Hz) was applied to account for the low-frequency distortion caused by the signal conditioner and ADC used in the acquisition process. A second-order, pole-zero inverse filter was applied to correct for the high-frequency response of the BRÜEL & KJÆR

hydrophones as specified by the manufacturer's datasheet. This latter filter assumed a minimum-phase impulse response with an amplitude correction ranging from 0.3 dB at 10 kHz to 2.9 dB at 22 kHz. In the second stage, the frequency regimes of the data containing no measurable airgun signal were removed using a filter with a low cut of 2 Hz and a high cut that was determined by the alias-free bandwidth of the ADC (i.e., 40% of the sampling frequency for the dataset under consideration). The precise values of the high-cut frequencies were rounded down to match the standard decidecade bands (IEC, 2016). (A decidecade is one-tenth of a decade. One-tenth of a decade is approximately equal to one-third of an octave and for this reason, it is sometimes referred to as a "one-third octave.")

V. CALCULATION OF SOURCE WAVEFORMS

In this section, we summarize the main steps in the conversion of the sound pressure $p(t)$ to the source waveform. For each emission and each available hydrophone channel of the corner and center array (see Fig. 3 for the geometry), there is one recording of $p(t)$. This recording is converted to the source waveform using a modified version of the method given by Ziolkowski *et al.* (1982) and described by Laws *et al.* (1998).

The airgun output is measured by a hydrophone placed nearby. The signal received by this hydrophone includes the direct signal from the airgun and the reflected signal from the sea surface (the ghost). In addition, it includes the reflection from the seabed and the entire seismogram, but these last two are small enough to be neglected.

The method proposed by Ziolkowski *et al.* (1982) removes the ghost signal from the hydrophone measurement by subtracting an approximation to it, which is obtained either iteratively or recursively, from the output source waveform and method of images. The source waveform is calculated from the deghosted hydrophone measurement using the assumption that the source is a monopole.

The method relies on the knowledge of the position of the hydrophone relative to the airgun and sea surface. In particular, the travel time difference and range difference between the direct and surface-reflected paths are significant. The surface-reflected signal must be subtracted from the hydrophone measurement so that what remains is simply the direct signal from the airgun to the hydrophone. From this "deghosted" pressure measurement, it is straightforward to calculate the source waveform.

The sound wavelengths at the higher end of the measured spectrum are much smaller than those typically of interest in seismic imaging and for which the methods given above were devised. However, up to about 2 kHz, the deviation of the bubble from the spherical is small compared with the wavelength. It is, therefore, reasonable to approximate its wavefield, at distances that are large compared with the bubble radius, as being that of a monopole. Furthermore, the sound wavelengths up to about 2 kHz are large compared with the amplitude of the waves on the sea surface during the experiment. It is, thus, acceptable to approximate the

J. Acoust. Soc. Am. **150** (5), November 2021

Prior *et al.*   3679

ghost effect as being due to a flat sea surface with a reflection coefficient of minus one.

In the case of a cluster of airguns, the deviation from the sphericity of the combined bubble will be significant at a lower frequency, perhaps around 200 Hz. Sound at 200 Hz has a wavelength of about 7.5 m, and the airguns in a cluster are typically 1 m apart.

For the frequencies higher than about 2 kHz, there might be significant deviations from the spherical behavior and planar surface scattering; it is impossible to cater for these in the processing, but they are implicitly included in the variation in the source waveform, which is derived from the hydrophones at different positions and for repeated emissions from the same airgun: the bubble shape is not the same for each repeated emission, nor is the sea surface shape.

To remove the surface reflection from the hydrophone measurement, it is necessary to know both the travel time and amplitude of the surface-reflected signal as it arrives at the hydrophone, both of which depend on the path length. If the hydrophone is close to the airgun, then the determined path length is important because the errors affect the amplitude of the surface-reflected signal. If the hydrophone is remote relative to the airgun, then the path length is important because the errors affect the arrival time of the surface-reflected signal. In addition, if the hydrophone is close to the airgun, the surface-reflected signal is much smaller in amplitude relative to the direct signal, hence, errors in it are less significant than they are for a more remote hydrophone where the surface-reflected signal might not be so small relative to the direct signal. The SV data extend to much higher frequencies than needed for geophysical processing. This means that positioning accuracies acceptable for seismic data acquisition are inadequate when the higher frequencies are included in the study.

In the SV dataset, there were both near-field hydrophones and more remote hydrophones, but for reasons discussed in Sec. III, the near-field hydrophones were not suitable for analysis. It was also found that the uncertainty of the positions of the more remote hydrophones was such that they required adjustments because of the travel time errors. Therefore, a processing method was developed that corrected the difference between the direct and surface-reflected path lengths. The path length difference was corrected using information about the expected shape of the source waveform: the airgun source waveform is known to be smooth as the pressure falls from its initial peak value. An incorrect path length difference leaves remnants of the ghost present at the point in the waveform that corresponds to the surface-reflected arrival. These remnants are a form of processing noise and often appear in the form of a diminished ghost arrival or as a ringing effect, i.e., a "saw tooth" waveform. The minimization of these remnants is used to optimize the correction to the path length.

A numerical grid search on a 30-point grid that runs from -0.7 to 0.7 ms was performed to determine this time delay (Ainslie et al., 2020). See Fig. 4 for an example of the
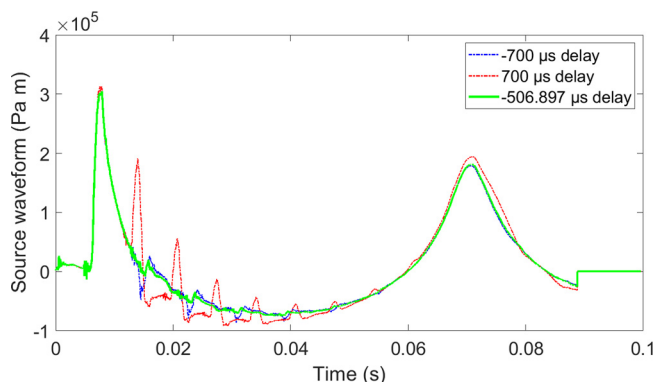

FIG. 4. (Color online) The source waveform $s(t)$ for the different time delays to correct for errors in the path length estimation that would otherwise result in an insufficient removal of the ghost arrival. The green trace shows the optimal result, whereas the blue and red traces show the lower and upper boundary of the grid, respectively. The airgun considered was a Bolt 1500 airgun; volume, 80 in.^{3} (1.31 L); depth, 8 m; and pressure, 1900 lbf in.$^{-2}$ (13.10 MPa).

grid search for one of the source signatures. This optimization does not always succeed in removing the remnants of the ghost entirely.

Despite the mitigating steps, a remnant of the saw tooth pattern remained after processing in some of the sequences. This saw tooth was an artefact and inevitably contained unwanted high-frequency noise that was not part of the source waveform. The quality of the resulting source waveform(s) was quantified by calculating the signal-to-processing-noise ratio (SPNR) for each sequence. The higher the SPNR, the greater our confidence in the inverted source waveform. For each test sequence, the source waveforms were computed for each shot-channel combination. Any faulty shot-channel combinations were rejected by excluding all signatures that deviated more than the median of the absolute differences ($L1$ norm) with respect to the median of the signatures of every sequence. The $L1$ norm is preferred because of its relative insensitivity to outliers. To further reduce any remaining processing artefacts, we proceed by taking the arithmetic mean over the peak-aligned channels for every emission recorded. Of this result, all signatures that deviated more than the median of the $L1$ norm with respect to the median of the averaged channels were also excluded. To obtain a single representative source waveform for each sequence, the emission was selected that was closest, in an $L1$-norm sense, to the per-sample median over all of the emissions. In this context, "median" does not mean a simple sample-by-sample median, which could introduce discontinuities in the waveform, instead it means the measured waveform that is closest to a sample-by-sample median. This postprocessing procedure results in a single representative mean source waveform with minimal processing artefacts.

All of the averaging options are presented in Fig. 5. The median of medians (abbreviated as med, med) selects one representative source waveform measurement (the result of a single physical experiment). We chose the average of medians (av, med) because this obtains a higher signal-to-noise ratio

3680   J. Acoust. Soc. Am. **150** (5), November 2021
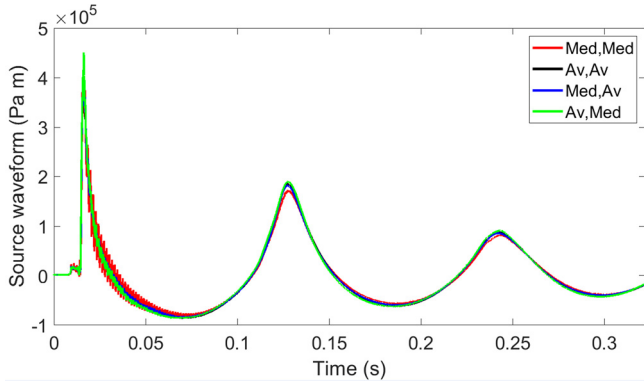
Prior et al.

FIG. 5. (Color online) The results of four different selection procedures are compared for the final source waveform. The attributes of this experiment are gun type, Bolt 1500; volume, 150 in.^{3}(2.458 L); depth, 2 m; and pressure, 2000 lbf in.$^{-2}$(13.79 MPa). The SPNR is 18.8 dB.

(SNR) by averaging over the channels as is shown when comparing the green (av, med) to the red trace (med, med) in Fig. 5. Furthermore, the median over emissions is preferred to the mean (av, med) for two reasons. First, during the first few emissions, the temperature of the airgun and surrounding water is expected to increase until a stable value is reached. The median is representative of this stable value. Second, when the first emission of a sequence is fired, the surrounding water will contain few, if any, bubbles. The density of the bubbles will increase with the number of emissions until a stable value is reached. The median is representative of this stable value.

All of the metrics were computed for the mean source waveform for each emission, and the statistics (the median, mean, and standard deviation of the logarithm of each metric) were computed over the emissions to quantify the emission-to-emission variation. The values of the metrics can depend on the frequency band in which the data are measured. The dataset under consideration here (Prior, 2018) was measured at one of three different sampling rates, 100 kHz in 2007 and 102.4 kHz or 51.2 kHz in the subsequent years, depending on the number of channels in use. To allow for comparison with the results of other research (e.g., Vaage *et al.*, 1983), three frequency bands were used. Two of these frequency bands used the same nominal low-cut frequency of 2.8 Hz but differed in the high-cut frequency. One nominal high-cut frequency was set to 141 Hz (to approximate a typical processing band for the geophysical imaging), and this band is hereafter called the "seismic band" (SB). The second band spans four decades with the low-cut frequency at 2.8 Hz and had a high-cut frequency of 28 kHz to obtain a frequency band spanning precisely four decades, and this is hereafter called the SV four-decade band. The third band uses an intermediate (three-decade) frequency range from around 8.9 Hz to 8.9 kHz, one of a set of standard frequency bands proposed by the Atlantic Deepwater Ecosystem Observatory Network (ADEON) and referred to as the "ADEON band" (BD; Ainslie *et al.*, 2018b). The results for bands with high-cut frequencies of 17.8 and 35.5 kHz and the same low-cut frequency as the SV-band showed no significant differences, indicating little source energy above 17.8 kHz, compared to the energy below this frequency. Examples of how the values of the metrics varied with the measurement band are given in Table II.

The variation of the metric values with the measurement band is most marked for the rise time variables where the time taken to rise between 10% and 90% of the peak waveform value is approximately four times greater for the SB band than for the SV. This is a straightforward consequence of SB's lack of high-frequency components, which are present in the SV-band. The variation with the band is less for other metrics with a peak source waveform and primary-to-secondary bubble-amplitude ratio in the SB band reducing by approximately 30% of their value in the BD band. All other metrics change by less than 15% between the BD and SB bands.

The relationship between some acoustic metrics and the airgun chamber pressure (P), volume (V), and operating depth (D) has been studied previously (Vaage *et al.*, 1983). These relationships are useful as predictive tools and also provide a validation of the derived metrics. That is, it would be expected that the dependence of the peak source waveform, for example, and P, V, and D should be broadly similar to the previously derived relationships for a comparable frequency band. The high-cut frequency used by Vaage *et al.* (1983) was 128 Hz. The power-law relations were

TABLE II. The geophysical imaging metrics and high-cut frequencies for sequence 100; for the Bolt 1500, 80 in.^{3} (1.31 L), 8 m depth, 1900 lbf in.$^{-2}$ (13.10 MPa). ddec refers to decidecade.

Band	BD	SV	SB	
Low-cut	ddec-20 (8.9125 Hz)	ddec-25 (28.184 Hz)	ddec-25 (28.184 Hz)	
High-cut	ddec 9 (8912.5 Hz)	ddec 14 (28.184 Hz)	ddec-9 (141.25 Hz)	
Metric (symbol)				Units
Peak source waveform (s_{pk})	289^{+8}_{-8}	287^{+9}_{-8}	194^{+7}_{-7}	kPa m
Total energy source factor ($F_{S,E,tot}$)	620^{+56}_{-51}	626^{+57}_{-52}	599^{+56}_{-51}	kPa^2 m^2 s
Root mean square (rms)source waveform, 1 ms averaging ($s_{rms,1 ms}$)	280^{+8}_{-8}	276^{+8}_{-8}	242^{+9}_{-9}	kPa m
Primary-to-secondary bubble-amplitude ratio (rPB)	$1.70^{+0.04}_{-0.04}$	$1.71^{+0.04}_{-0.04}$	$1.19^{+0.01}_{-0.01}$	—
Rise time 1: first 10% to first 90% value ($\tau_{s,rise,1}$)	$0.857^{+0.049}_{-0.046}$	$0.851^{+0.044}_{-0.041}$	$3.24^{+0.72}_{-0.59}$	ms
Rise time 2: last 10% to first 90% value ($\tau_{s,rise,2}$)	$0.857^{+0.049}_{-0.046}$	$0.851^{+0.044}_{-0.041}$	$3.13^{+0.00}_{+0.00}$	ms
Bubble period τ_B	$62.4^{+0.4}_{-0.4}$	$62.4^{+0.4}_{-0.4}$	$61.1^{+0.5}_{-0.5}$	ms

J. Acoust. Soc. Am. **150** (5), November 2021

Prior *et al.*   3681

sought between P, V, D, and two metrics: the peak source waveform, S_{pk}, and the total energy source factor, $F_{S,E,\text{tot}}$. These metrics were selected as being two fundamental descriptors, measuring the highest value of the waveform and its total energy content.

Following Vaage et al. (1983), polynomial relationships were derived for single airguns but not for clusters. The results for "injector" guns were also excluded. These devices discharge air in two phases, an initial release followed by a secondary release, designed to impede the bubble collapse and, hence, remove the bubble peak from the source waveform. This process alters the relationship between the acoustic metrics and chamber volume, making them distinct from other airguns.

Relationships of a form similar to those used previously by Vaage et al. (1983) were sought. Specifically, the fits were made between metrics and the product of the three descriptors, each being raised to a unique power. The following trend was found for the peak waveform value:

$$s_{pk}^2(P,V,D) \approx 1368^{+520}_{-377}\,\text{kPa}^2\,\text{m}^2 \left(\frac{P}{1\,\text{MPa}}\right)^{1.52\pm0.12}$$
$$\times \left(\frac{V}{1\,\text{L}}\right)^{0.65\pm0.06} \left(\frac{D}{1\,\text{m}}\right)^{-0.06\pm0.05}, \quad (1)$$

and for $F_{S,E\,\text{tot}}$,

$$F_{S,E,\text{tot}}(P,V,D) \approx 37.1^{+14.1}_{-10.1}\,\text{kPa}^2\,\text{m}^2\,\text{s} \left(\frac{P}{1\,\text{MPa}}\right)^{1.13\pm0.11}$$
$$\times \left(\frac{V}{1\,\text{L}}\right)^{0.89\pm0.05} \left(\frac{D}{1\,\text{m}}\right)^{-0.23\pm0.04}. \quad (2)$$

The uncertainties quoted in Eqs. (1) and (2) are expressed in terms of one standard deviation about the estimated mean values.

It is common for logarithmic measures of these metrics, $L_{S,pk}$ and $L_{S,E}$, to be used and when converting to decibels, the same relationships become

$$L_{S,pk} \approx 211.4\,\text{dB} + 15.2\,\log_{10}\frac{P}{1\,\text{MPa}}\,\text{dB}$$
$$+ 6.5\,\log_{10}\frac{V}{1\,\text{L}}\,\text{dB} - 0.6\,\log_{10}\frac{D}{1\,\text{m}}\,\text{dB}, \quad (3)$$

$$L_{S,E} \approx 195.7\,\text{dB} + 11.3\,\log_{10}\frac{P}{1\,\text{MPa}}\,\text{dB}$$
$$+ 8.9\,\log_{10}\frac{V}{1\,\text{L}}\,\text{dB} - 2.3\,\log_{10}\frac{D}{1\,\text{m}}\,\text{dB}. \quad (4)$$

Using customary units for the pressure, volume, and depth allows Eqs. (3) and (4) to be rewritten, respectively, as

$$L_{S,pk} \approx 166.9\,\text{dB} + 15.2\,\log_{10}\frac{P}{1\,\text{lbf/in.}^2}\,\text{dB}$$
$$+ 6.5\,\log_{10}\frac{V}{1\,\text{in.}^3}\,\text{dB} - 0.6\,\log_{10}\frac{D}{1\,\text{m}}\,\text{dB}, \quad (5)$$

$$L_{S,E} \approx 155.5\,\text{dB} + 11.3\,\log_{10}\frac{P}{1\,\text{lbf/in.}^2}\,\text{dB}$$
$$+ 8.9\,\log_{10}\frac{V}{1\,\text{in.}^3}\,\text{dB} - 2.3\,\log_{10}\frac{D}{1\,\text{m}}\,\text{dB}. \quad (6)$$

The scatterplots illustrating Eqs. (5) and (6) are shown, respectively, in Figs. 6 and 7 in which the measured and curve-fit values are displayed. The data are shown to cluster around the $y = x$ line on which they would all fall if the power-law fit were precise. The standard deviations of the errors were found to be less than 2 dB in both cases and Figs. 6 and 7 show dashed lines drawn at ± 3 standard deviations from the $y = x$ line.

Vaage et al. (1983) performed a series of far-field measurements of the emitted pulse from single airguns. Their measurements were made over the seismic frequency range, whereas our measurements are full-band. Vaage et al. (1983) also showed how certain metrics of the far-field pulse depend on the pressure, volume, and depth of the airgun. The far-field peak should behave in a similar way to the source waveform peak, therefore, a direct comparison between our results and those of Vaage et al. (1983) for this quantity is instructive.

The peak source waveform (s_{pk}), referred to as 'Amplitude' in (Vaage et al., 1983), was observed in their tests to follow

$$s_{pk}(P,V,D) \propto P^{3/4}V^{1/3}D^0. \quad (7)$$

Squaring this relation and converting the exponents from fractions to decimals gives

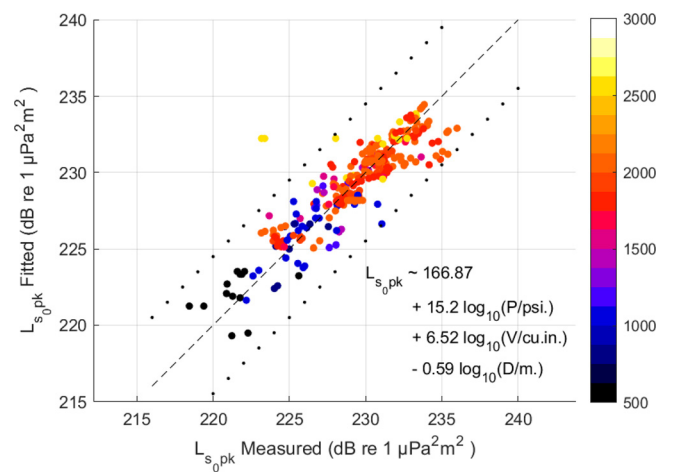$$s_{pk}^2(P,V,D) \propto P^{1.50}V^{0.67}D^{0.00}. \quad (8)$$

FIG. 6. (Color online) A scatterplot of the measured values for the metric $L_{S,pk}$ re 1 μPa m (dB) on the x axis plotted against values of the same quantity inferred from the curve-fitting procedure using the chamber pressure, chamber volume, and deployment depth. The straight line shows $y = x$. The statistics for the GI gun and clusters are excluded from this analysis. The colors correspond to the chamber pressure in lbf/in.^{2}. The dotted lines are three standard deviations from the trend line.
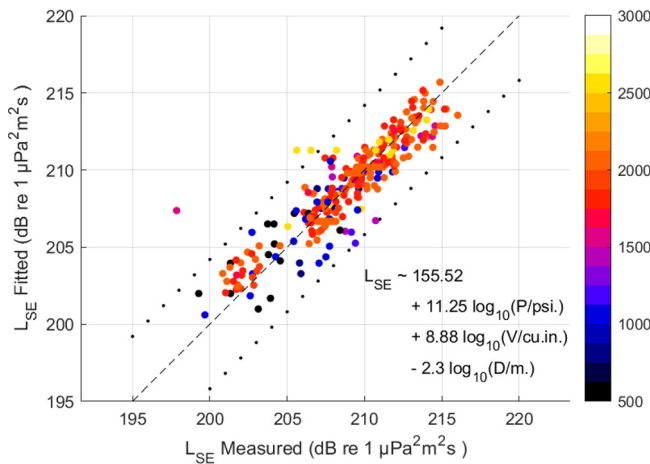
3682   J. Acoust. Soc. Am. 150 (5), November 2021

Prior et al.

FIG. 7. (Color online) A scatterplot of the measured values for the metric $L_{s,E}$ re 1 μPa^2 s (dB) on the x axis plotted against values of the same quantity inferred from the curve-fitting procedure using the chamber pressure, chamber volume, and deployment depth. The straight line shows $y = x$. The statistics for the GI gun and clusters are excluded from this analysis. The colors correspond to the chamber pressure in lbf/in.^{2}. The dotted lines are at three standard deviations from the trend line.

Thus, the P and V exponents reported by Vaage *et al.* (1983) are within the 95% confidence limits of our results, whereas their D exponent is just outside of these. Vaage *et al.* (1983) do not provide confidence bounds, but it seems likely that they would be no smaller than those obtained with this larger dataset, making the differences insignificant. The results reported in this paper are, therefore, consistent with the results of Vaage *et al.* (1983).

VI. VALIDATION

The source waveforms derived using the method described in Sec. V were validated by a comparison between the sound pressure signals measured at deep hydrophones in the SV dataset and pressures predicted using the source waveforms. This prediction was calculated via two approaches. The first approach was to use the method of images (Jensen *et al.*, 2011). The sound pressure calculated by the method of images is referred to as the "reconstructed sound pressure." A second pressure-prediction was made using the surface-affected source waveform (ISO, 2017). This alternative description of the acoustic output of airguns is also known as the "far-field signature" and is a widely used descriptor for the acoustical output of airguns (Johnston *et al.*, 1988). It is the product of the distance from the airgun and the far-field sound pressure that would be measured at that distance below the airgun in a hypothetical semi-infinite uniform lossless medium of the same density and sound speed as the actual medium at the location of the source. The "semi-infinite" medium includes the sea surface, and the surface-affected source waveform, therefore, includes the surface ghost, i.e., the contribution of paths that are reflected from the surface before propagating down to the receiver location. In this scenario, the distance of the receiver should be large compared to the airgun depth. Thus, the real and reflected sources are at, effectively, the

same distance from the receiver with regard to the amplitude, although not, of course, with regard to the travel time delay. The pressure at deep hydrophones was calculated by dividing the surface-affected source waveform by the source-receiver distance to yield the "convolution sound pressure." This second estimate of the pressure was calculated in recognition of the fact that the surface-affected source waveform of an airgun is a commonly used descriptor. Validation of this process would be of direct interest to many practitioners in the field, allowing them to relate the validation process directly to a descriptor with which they are familiar.

In theory, the sound pressures calculated by these two methods should be very similar. However, practical issues may introduce slight differences. For example, the surface-affected waveform is calculated in the far-field so that the distance between the airgun and receiver is assumed to be the same as the distance between the receiver and the negated image of the receiver in the sea surface. This assumption becomes more accurate at larger distances. The deepest hydrophone in the SV dataset was at a depth of 100 m and this was used for all of the cases in which such a hydrophone was present. However, for some sequences in the dataset, the deepest receiver was not operational and in these cases, a second hydrophone was used, which was located at a depth of 30 m. The maximum airgun operating depth studied was 25 m and in sequences with this airgun depth, the reconstructed and convolution pressures may differ significantly.

The selected methodology for comparison used scatterplots showing metrics describing the measured and predicted pressures. The values of the metrics from the measurements were displayed on the x axis and values of the metrics from the predicted pressure were displayed on the y axis. These allow data for all gun/pressure/depth combinations to be displayed in a single figure. Good agreement was indicated by tight grouping about the $y = x$ line. The amount of mismatch may be put into context by comparison with the spread of values for the measurement metrics. This spread is referred to as the repeatability of the measurements, i.e., the spread of measured values observed over a sequence of emissions in which gun type, chamber pressure, and deployment depth were held constant, and the metric values might reasonably be expected to vary only as a result of the uncontrolled experimental factors.

A. Comparison of reconstructed and convolution pressures

Figure 8 shows the sound exposure level (SEL) $L_{E,p}$ (ISO, 2017), which is the level of the time-integrated squared sound pressure expressed in decibels and a measure of the total acoustic energy per unit area at a receiver. In general terms, $L_{E,p}$ calculated from the pressures predicted by both methods agreed well with each other, as indicated by the close spacing of the up- and down-pointing triangles. The repeatability of the metric values derived from the measured sound pressures was observed to be good, and the
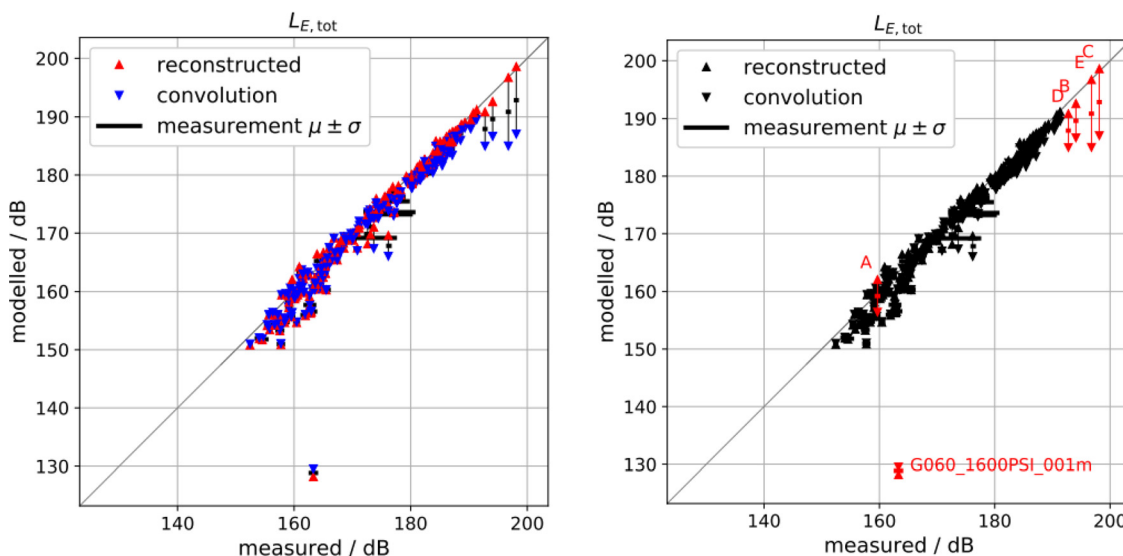
FIG. 8. (Color online) (A) The total broad SV-band (2.8 Hz–28 kHz) sound exposure level (SEL; $L_{E,p}$ re 1 μPa^2 s) and comparison between the measurements with the modelled signals. The upward-pointing triangles indicate the metrics produced using the source waveforms, each being connected by a line to a downward-pointing triangle, indicating the metric calculated for the same sequence but using the surface-affected source waveform. The repeatability (spread within measured sequences) is indicated by the horizontal black bars but is often so small that those bars appear to be dots, cf. points at the extreme top right of the left panel. (B) The same data is shown with labels attached to the sequences displaying poor agreement either between the measured and predicted pressures or between the reconstructed and convolution pressures.

horizontal bars showing this spread in Fig. 8 are often not visible.

The predicted values of $L_{E,p}$ generally agree well with the values produced from the measured data, as indicated by the close grouping of most points around the $y = x$ line. The sequence G060_1600PSI_001m was an anomalous sequence associated with a very low SPNR. Six other sequences, which had convolution pressures that were also unusually far from the $y = x$ line, are highlighted and labelled in the right-hand panel of Fig. 8. Details of the other five sequences are given in Table III.

Outlier A corresponds to a very shallow source with one of the lower chamber pressures used. The low time-separation between the direct path and ghost is the likely source of the differences observed. All of the other outliers (B–E) in Table III correspond to clusters being fired at a relatively great depth (25 m), whereas the receiver at which the pressure was measured was relatively shallow (30 m instead of 100 m). Because the measured and modelled pressures were observed to be similar for other source clusters, it is inferred that the greater difference between modelled pressures in the labelled cases is not simply the result of these

sequences corresponding to clusters. Rather, it is thought to be due to the proximity of the source and receiver.

Figure 9 shows a scatterplot of the measured and predicted peak levels of the total pressure in the broad SV-band (2.8 Hz–28 kHz). The trends observed for this metric are similar to those previously observed for the SEL. For 97% of the sequences, the absolute difference between the reconstruction and mean measured was less than 3 dB.

In summary, the comparison of the reconstructed and convolution pressures showed that the difference between the two was generally less than 5 dB. This indicated that the "predicted" pressure at the far-field hydrophones (100 and 30 m) was generally independent of which approach was used. The following sections refer to the "modelled pressure" without further distinction between the two methods.

B. Comparison of the frequency-weighted measures of sound exposure

The sound exposure values shown in Fig. 8 were calculated without the application of any frequency weighting. Such weightings are often used when assessing the potential impact of underwater sound on species of marine life whose

TABLE III. The list of sequences for which the differences between the two model predictions are greater than 5 dB. The letters in the first column refer to the labels in Fig. 8.

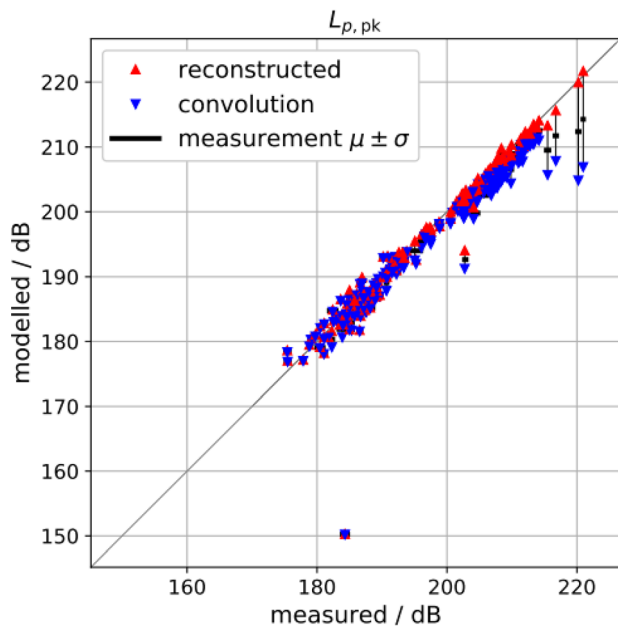| Label	Year	Model	Chamber volume (L)	Depth (m)	Firing pressure (MPa)	Description	Receiver depth (m)
A	2007	G-gun	4.097	1	6.895	Single gun	100
B	2010	Bolt 1500	4.916	20	13.79	Cluster (80 cm separation)	30
C	2010	Bolt 1500	4.916	25	13.79	Cluster (80 cm separation)	30
D	2010	Bolt 1900	4.097	20	13.79	Cluster (80 cm separation)	30
E	2010	Bolt 1900	4.097	25	13.79	Cluster (80 cm separation)	30

FIG. 9. (Color online) The level of the broad SV-band (2.8 Hz–28 kHz) peak sound pressure ($L_{p,\mathrm{pk}}$ re 1 μPa^2) in dB and comparison between the measurement and the reconstructed signals. The upward-pointing triangles indicate the metrics produced using the source waveforms, each being connected by a line to a downward-pointing triangle, indicating the metric calculated for the same sequence but using the surface-affected source waveform. The repeatability (spread within measured sequences) is indicated by the horizontal black bars.

hearing sensitivity varies with the frequency (NMFS, 2018; Southall *et al.*, 2019). Acoustic emissions of airguns are concentrated at frequencies on the order of tens of hertz. Agreement in the predicted and measured values of $L_{E,p}$ is indicative of the two waveforms being similar in this band of peak energy output but does not guarantee that the signals are similar at all frequency bands.

Figure 10 shows scatterplots of the measured and predicted metrics of the SEL for various frequency bands. The top left panel has no frequency weighting applied and these data, the same as those shown in Fig. 8, are included here only to allow ease of comparison between the results of the different weightings. All of the other bands are specific to particular hearing groups' auditory frequency weighting functions, summarized in Table IV and taken from NMFS (2018) for Figs. 10(a)–10(f) and from Southall *et al.* (2019) for Figs. 10(g) and 10(h).

Agreement between the metrics derived from the measured and predicted pressures is generally good for the cases in Figs. 10(a)–10(d) and is summarized in Table V.

Good agreement was not observed for all of the frequency weightings. Figures 10(e)–10(f) show poor agreement between the modelled and measured SELs calculated using the frequency weightings appropriate for medium-frequency and high-frequency cetaceans from NMFS (2018). The nature of this disagreement highlights a feature of the metric calculation rather than indicating a weakness in the source data.

The measured data points for the National Marine Fisheries Service (NMFS)-weighted results are grouped around values slightly below 130 and 140 dB re 1 μPa^2 s. Figure 11 shows the same data as in Figs. 10(e) and 10(f) but with markers that are color-coded by measurement year. This illustrates that the groups are strongly correlated with the year in which the data were gathered with the lower measured values corresponding mainly to 2007 and the higher values corresponding with 2009/2010. This behavior is consistent with a situation in which the measured data are significantly affected by background noise. The narrow grouping on the *x* axis and wider spread on the *y* axis indicates that the measured SEL was not particularly dependent on the gun type, chamber pressure, and operating depth. This is consistent with the measured data being dominated by the ambient noise or system self-noise rather than the airgun emissions.

Figures 10(g) and 10(h) show comparisons of the metrics for the medium-frequency and high-frequency cetaceans using the "*M*-weighting" (Southall *et al.*, 2007). These comparisons demonstrate good model-measured agreement, indicating that the contamination by noise for the medium- and high-frequency-cetacean metrics, suggested in Figs. 10(e) and 10(f), is a consequence of a combination of the greater emphasis placed on higher frequencies by the NMFS weightings and the reduced energy emitted by airguns at these frequencies. Table VI shows the low and high cut-off frequencies used in the two weightings, and it is shown that the NMFS weightings place a reduced weighting on sound below 8.8 kHz for the medium-frequency cetaceans and below 12 kHz for the high-frequency cetaceans.

Figure 12 shows the frequency spectra of the SEL, calculated in decidecade bands for the pressure signals received at the corner hydrophone array (left) and center array (right). The left-hand panel shows that the data recorded on the corner hydrophone array (closer to the source) have a high SNR over a band spanning from a few hertz to more than 10 kHz. These measurements were used to produce the source characterizations, and this high SNR indicates that those characterizations describe the airgun output at those frequencies. The right-hand panel, however, shows that at the deeper receiver, the SNR is high only over a restricted frequency band and above 10 kHz, the signal has fallen below the noise. The metrics calculated in those years are consequently correlated with the noise (and, therefore, measurement year) rather than with the airgun characteristics.

This situation is a consequence of the fact that the metrics for the sound exposure in all of the bands were calculated using a common period for the time-integration of the squared-pressure. This period was chosen to be the duration of the SV-band (2.8 Hz–28 kHz) signature. However, it is commonly seen (Coste *et al.*, 2014) that the high-frequency components of an airgun's emissions are associated with the earliest parts of the waveform, generated by the initial release of air. Thus, if the time-integration is extended beyond this, there is little or no increase in the high-frequency signal content; however, high-frequency noise components will rise linearly with the duration of the temporal observation window. Consequently, there will be an
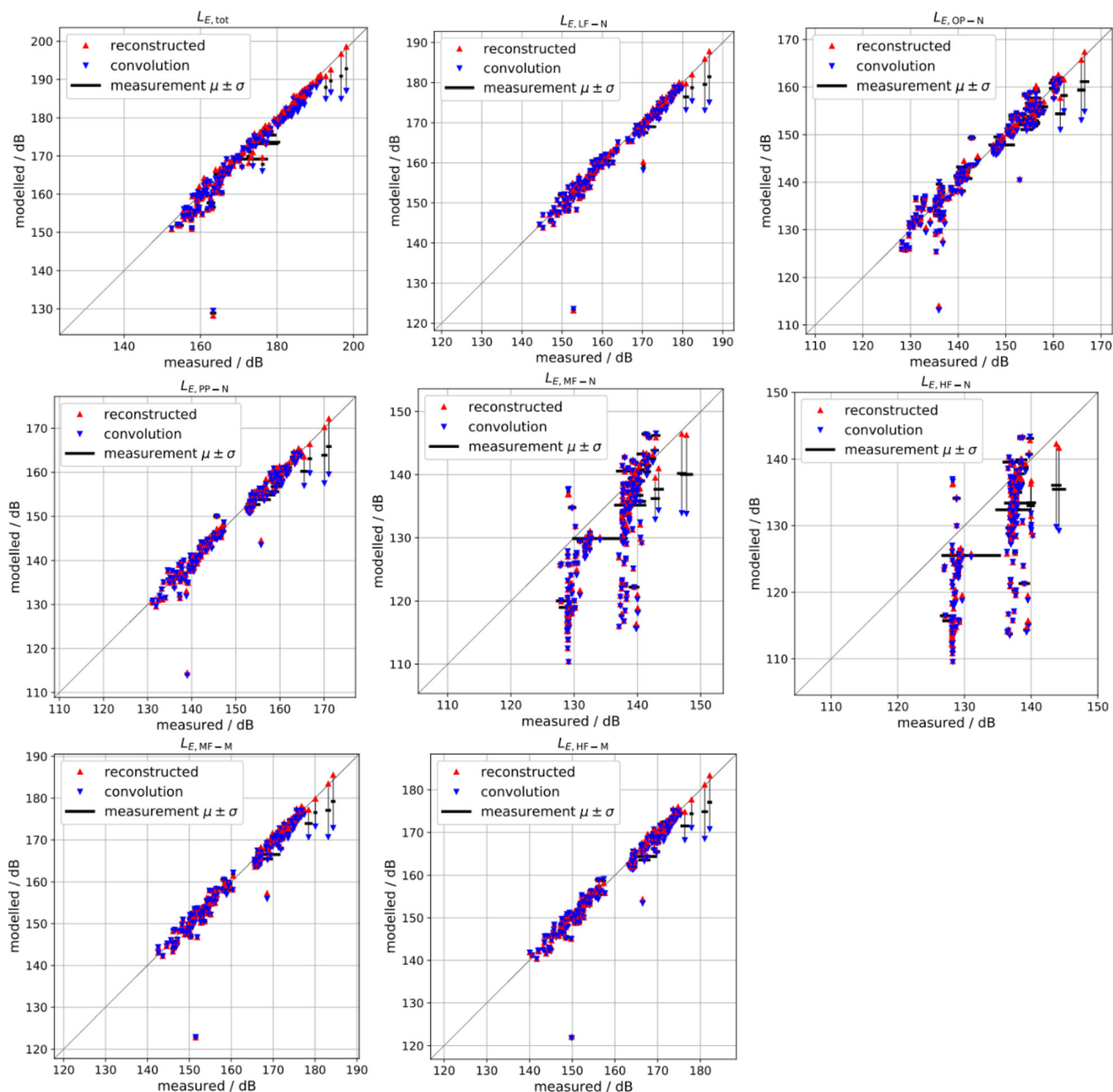
J. Acoust. Soc. Am. **150** (5), November 2021

Prior *et al.*   3685

FIG. 10. (Color online) The model-measured comparison for various frequency-weighted measures of the received SEL (re 1 μPa^2 s). (A) The broad SV-band (2.8 Hz–28 kHz); (B) the low-frequency cetaceans (NMFS, 2018); (C) the otariidae pinnipeds, e.g., sea-lions (NMFS, 2018); (D) the phocidae pinnipeds, true seals (NMFS, 2018); (E) the medium-frequency cetaceans (NMFS, 2018); (F) the high-frequency cetaceans (NMFS, 2018); (G) the medium-frequency cetaceans (Southall *et al.*, 2007), and (H) the high-frequency cetaceans (Southall *et al.*, 2007) are shown.

integration period beyond which the high-frequency metrics become significantly affected by the background noise. The higher the frequency, the shorter the period at which this effect becomes apparent.

The dominance of the noise in the high-frequency NMFS sound exposure values [calculated using the duration of the SV-band (2.8 Hz–28 kHz) pulse] is an indication that most of the high-frequency energy is emitted during a small

TABLE IV. The naming of the hearing groups according to NMFS (2018) and Southall *et al.* (2019). The nomenclature of NMFS (2018) is followed here.

NMFS (2018)	Southall *et al.* (2019)	Example species
Low-frequency (LF) cetaceans	Low-frequency (LF) cetaceans	Blue whale
Mid-frequency (MF) cetaceans	High-frequency (HF) cetaceans	Bottlenose dolphin
High-frequency (HF) cetaceans	Very high-frequency (VHF) cetaceans	Harbor porpoise
Phocid pinnipeds (PW; underwater)	Phocid carnivores in water (PCW)	Harbor seal
Otariid pinnipeds (OW; underwater)	Other marine carnivores in water (OCW)	Sea lion

3686   J. Acoust. Soc. Am. **150** (5), November 2021

Prior *et al.*

TABLE V. The mismatch (model prediction minus mean of measurements) for the full-bandwidth and weighted sound exposures (excluding labelled outliers). N/A, not applicable.

Metric	Species Group	Reconstructed pressure		Convolution pressure	
		Mean mismatch (dB)	rms Mismatch (dB)	Mean mismatch (dB)	rms Mismatch (dB)
E_{tot}	N/A	-1.19	3.22	-1.90	3.50
$E_{LF,N}$	Low-frequency cetaceans	-0.57	2.59	-1.08	2.92
$E_{OP,N}$	Otariidae pinnipeds, e.g., sea-lions	-0.27	2.74	-0.81	3.20
$E_{PP,N}$	Phocidae pinnipeds, i.e., true seals	-0.46	2.34	-0.99	2.84

portion of the duration of the SV-band pulse. This is despite the fact that the measured signals were recorded at distances less than 100 m from the airguns considered.

C. Peak sound pressure level ($L_{p,pk}$) and moving-window maximum root mean square (rms) sound pressure level ($L_{p,rms}$)

The peak sound pressure level (or zero-to-peak sound pressure level) is a logarithmic measure of the maximum modulus pressure observed during the duration of a signal. Whereas SEL is a time-integrated measure, $L_{p,pk}$ is an instantaneous value and may, therefore, be expected to be a more "erratic" measurement in that it is likely to be more sensitive to random fluctuations between emissions within a sequence and sampling errors that vary between measurements, which should nominally be the same. For example, the average of the peaks is higher than the peak of the average over the channels.

The maximum windowed rms sound pressure level was calculated using two averaging windows: 1 ms and 100 ms. Because these two times were generally less than the duration of the signals under study, the rms values were calculated using a series of windows, starting at different samples of the signal. The largest value recorded for any window was used to give the reported value of $L_{p,rms}$.

The top panel in Fig. 13 shows $L_{p,pk}$ metrics for all of the sequences in the SV dataset. Agreement is shown to be generally good with the exception of the outliers, which has previously been discussed. The rms mismatch of levels is 0.04 dB when using the reconstruction algorithm ($\sigma = 1.54$ dB). Using the convolution algorithm, the mismatch is 0.72 dB ($\sigma = 2.27$ dB).

The other two panels in Fig. 13 show the maximum windowed $L_{p,rms}$ values calculated for averaging windows of 1 (top right) and 100 ms (bottom left). Agreement is, again, good with very similar patterns observed. The greater averaging window is shown to give generally lower rms values as would be expected for airgun signals, which usually show a large peak of sound pressure early on, the duration of which is generally less than 100 ms. The maximum rms sound pressure level for the smaller averaging window is shown to be very similar to $L_{p,pk}$.

The agreement between the measured and modelled peak and 1-ms-averaged rms sound pressures is a particularly encouraging validation of the source characterizations developed. The peak sound pressure is a time-singular descriptor, and the successful matching of it represents a greater challenge than a similar matching of a time-integrated descriptor such as SEL.

D. Signal spectra comparisons

Figure 14 shows the spectra of the pressure signal measured at a deep hydrophone and predicted using the
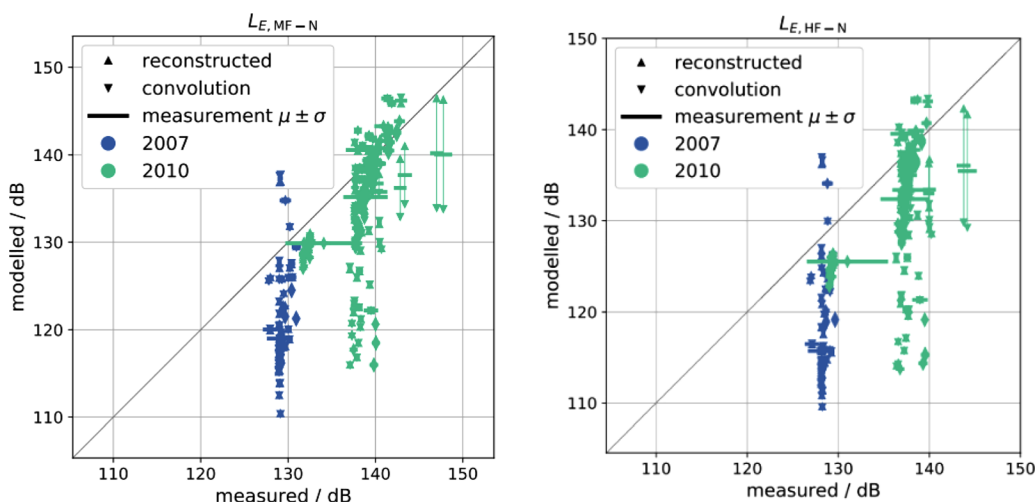

FIG. 11. (Color online) The model-measured comparison of the SEL (re 1 μPa^2 s) using the frequency weightings for the medium-frequency cetaceans (left) and high-frequency cetaceans (right) using the National Marine Fisheries Service (NMFS) weighting (NMFS, 2018). The markers are color-coded by measurement year.
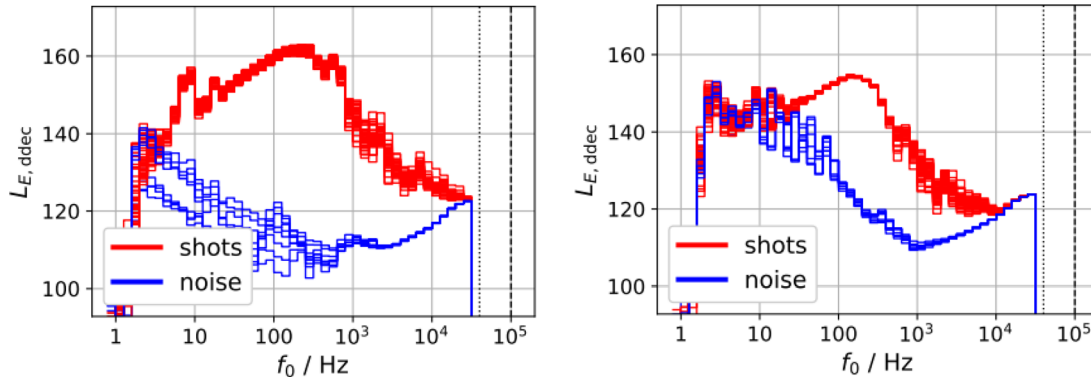
J. Acoust. Soc. Am. **150** (5), November 2021

Prior *et al.*   3687

FIG. 12. (Color online) The sound exposure calculated in dB re 1 μPa^2 s, calculated in decidecade bands for one data sequence for the receivers on the corner array of hydrophones (left) and the deeper, central hydrophones (right). The red lines ("shots"), signal + noise; blue lines ("noise"), noise.

reconstruction approach. Each spectrum is calculated by Fourier transforming the sound pressure signal to give a sound pressure spectrum. The modulus of this is then taken and squared to give an "exposure spectral density." Because the magnitude of the Fourier transform of the sound pressure signal is symmetric for positive and negative frequencies, only the positive frequencies are shown.

The measured data are shown in the form of a median level, taken over all emissions in the sequence made for a single gun type, constant pressure, and constant operating depth. The measurement repeatability is illustrated by the dotted and dashed lines showing the 10th and 90th percentiles, respectively, of the measured spectra over the sequence.

Figure 14 shows good agreement between the predicted and measured spectra for the sequence. The reconstructed spectrum lies within the repeatability of the measurements, and the locations of the peaks and troughs in the spectra are well matched. This good matching is present for all of the frequencies up to 1 kHz, beyond which the reconstructed data fall below the measured data. This is interpreted as being another manifestation of the effect discussed in Sec. VI B, where high-frequency components in measured data become influenced by noise as a result of the use of a time-window that is greater than the extent of the signal for which the high-frequency components are present.

At frequencies below 10 Hz, the measurement repeatability worsens, as indicated by the increasing spread of the 10th and 90th percentiles shown in Fig. 14. This effect was not always present, and Fig. 15 shows an example of a sequence in which it was absent.

Other sequences, however, showed this effect to a much greater degree, as illustrated by Fig. 16.

The mismatch at other frequencies in Fig. 16 is generally small compared to the measurement repeatability, and this is not suggestive of any breakdown in the prediction procedure, including the derived source waveform. In addition, the spectral content of the measurements below 10 Hz does not appear to be a good physical representation of the output of an airgun, which would be expected to fall with a decreasing frequency in this band. Figure 17 shows a shaded image representation of the stacked time-series from the same sequence of emissions. The color scale of Fig. 17 illustrates pressures much lower than the largest-amplitude peaks and troughs of the airgun signal itself, which are present after time-zero in the plot.

Figure 17 shows the pressure fluctuations of the periods corresponding to frequencies below 10 Hz. The fluctuations are present before and after the emission, suggesting that they are not a consequence of any sound or vibration induced by the airgun discharge. These fluctuations are hypothesized to be a result of the vertical motions of the measurement hydrophone, caused by the wave-induced motion of the platform from which the experimental equipment was deployed. This hypothesis is supported by the observation that poor measurement repeatability and high measured levels were observed only intermittently in the dataset. This suggests that the effect is a consequence of conditions peculiar to certain measurement periods rather than being a result of systematic measurement procedures or signal-processing strategies.

Figure 18 shows an example of a form of mismatch that was repeatedly seen in the dataset. At frequencies below 200 Hz, mismatch is generally low, and the reconstructed spectrum matches the level and detail of the measurements whose repeatability is good, notwithstanding a moderate level of motion-induced noise below 10 Hz. Above 200 Hz, however, the measured and reconstructed fields show similar levels, but the locations of their peaks and troughs no longer coincide. This is interpreted to be caused by a mismatch between the stated and actual depths of the source or receiver. The peaks and troughs in the data are caused by
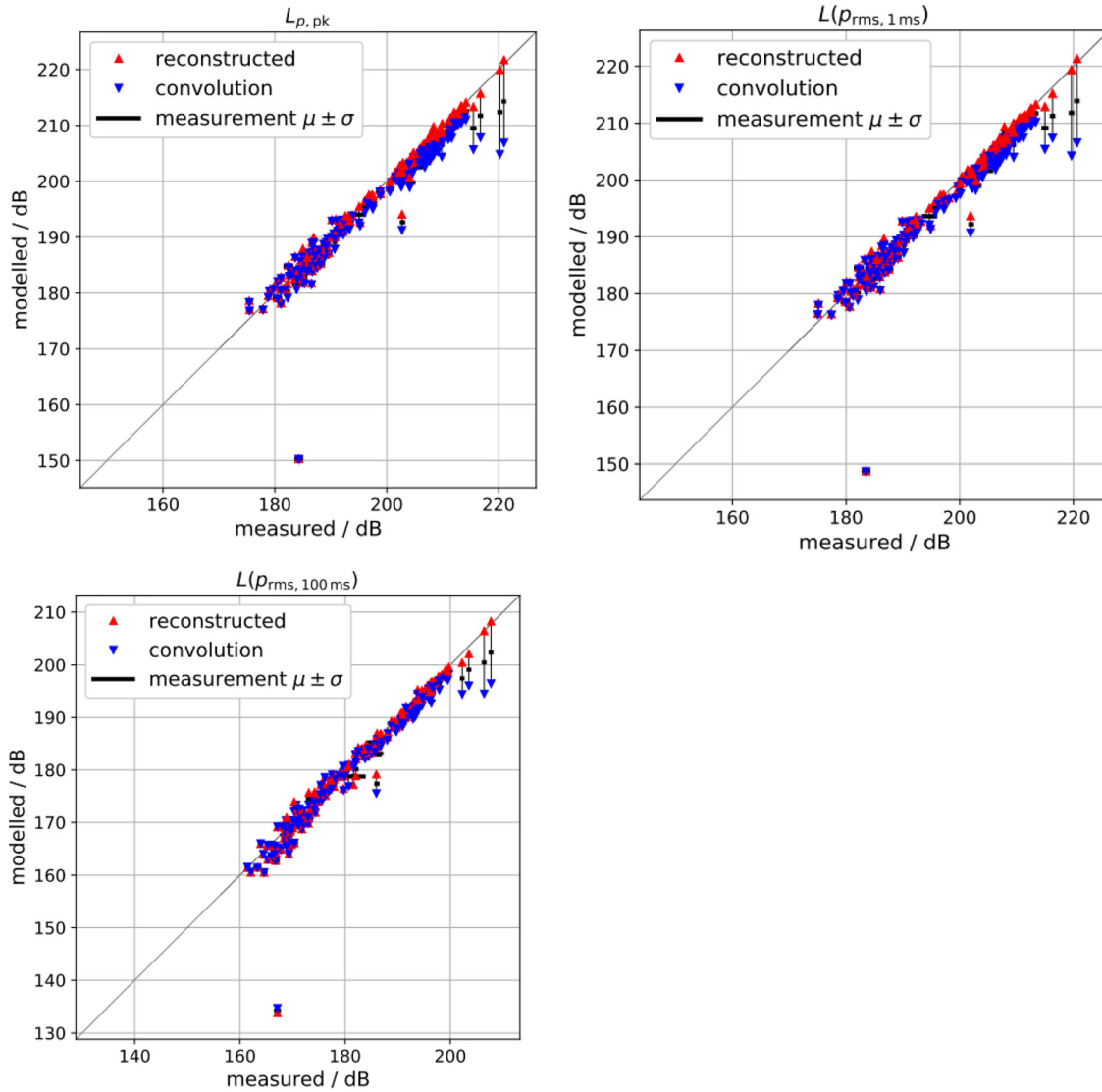
TABLE VI. The parameters for the low and high cut-off frequencies used in the weighting functions by Southall *et al.* (2007) (*M*-weighting) and NMFS (2018).

	Southall *et al.* (2007)		NMFS (2018)	
	f_{low}/Hz	f_{high}/Hz	f_{low}/Hz	f_{high}/Hz
Mid-frequency cetaceans	150	160 000	8 800	110 000
High-frequency cetaceans	200	180 000	12 000	140 000

3688   J. Acoust. Soc. Am. **150** (5), November 2021

Prior *et al.*

FIG. 13. (Color online) The peak sound pressure level (re 1 μPa^2) $L_{p,\text{pk}}$ (top left) and RMS sound pressure level $L_{p,\text{rms}}$ re 1 μPa^2 for the averaging periods of 1 ms (top right) and 100 ms (bottom left) for the measured and modelled signals.

interference between the direct and surface-reflected paths, and any change in the source or receiver depth will change the relative lengths of these paths, altering the frequencies at which their path differences result in destructive interference. The absence of this mismatch for some source depths suggests that it was the source whose depth was subject to experimental error rather than the receiver, which was not moved between sequences.

VII. DISCUSSION

The quality of the recorded data varied across the measurement sensors, and the analysis reported here was restricted to only those data of the highest quality. There remains the possibility that even more value could be extracted from the dataset if effort were to be expended in overcoming the difficulties in the calibration associated with some sensors. The poorest agreement between the pressures measured on the far-field hydrophones and those predicted using the source waveforms was observed for the metrics that placed emphasis on the highest frequencies (approximately more than 8000 Hz). At these frequencies, the airguns' acoustical emissions represent a very small part of their total energy output, and the emission is concentrated into periods much less than the duration of the signal recorded over the entire measurement band. This means that the integrated energy output calculated over the total duration is significantly affected by the background noise that is present for the duration of the signal. It could be argued that this illustrates that the airguns' acoustical output is not significant at these frequencies because the background noise is more energetic than the airgun signal during the period of emission. A counterargument is that the integration period should change with the frequency band of interest so that the signal and noise are compared only during times for which the airgun output is significant. This topic is

J. Acoust. Soc. Am. **150** (5), November 2021
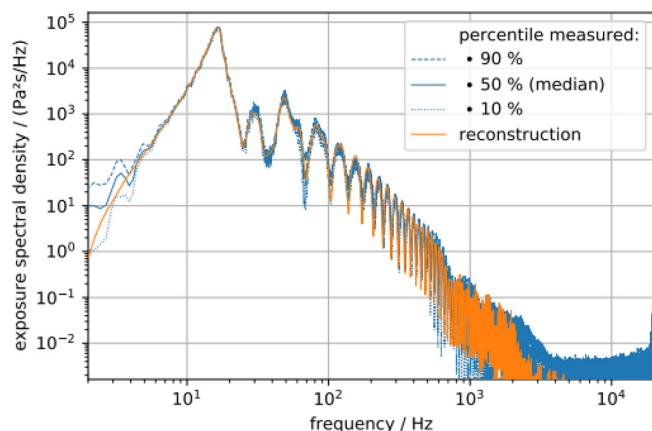
Prior *et al.*   3689

FIG. 14. (Color online) The exposure spectral density at a deep hydrophone measured (blue lines) and predicted by the reconstruction (orange line) for a G-gun of volume 250 in.[3] (4.10 L), operated at a chamber pressure of 2000 lbf/in.[2] (13.79 MPa) and deployed at a depth of 20 m.

FIG. 16. (Color online) The spectra of the pressure at a deep hydrophone measured (blue lines) and predicted by the reconstruction (orange line) for a Bolt gun of volume 150 in.[3] (2.46 L), operated at a chamber pressure of 1800 lbf/in.[2] (13.79 MPa) and deployed at a depth of 2 m.

particularly relevant to the calculation of the acoustical impact of the airguns on marine life species that are sensitive to high-frequency signals and is worthy of further investigation.

The metrics derived to describe the source waveforms, such as energy source level and peak source waveform, allow rapid comparisons to be made between the diverse airguns. The use of different analysis bands in the calculations of different sets of metrics allows them to be used in assessments of both their utility for seismic imaging and potential impact on marine life.

Experimental data showed variations in the signals recorded within the sequences, i.e., after multiple emissions of the same gun at the same depth and chamber pressure. This finite "repeatability" resulted in a similar spread in the source waveforms derived for each combination of gun type, chamber pressure, and deployment depth, and represents a "measurement uncertainty" of those waveforms. A single, representative source waveform was derived for each sequence by calculating a mean source waveform over all recording channels for each emission after rejection of the
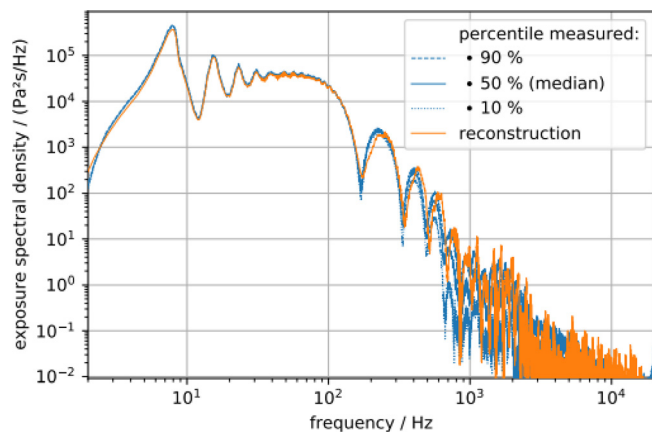
outliers. The resulting set of source waveforms, one for each emission in the sequence, was further reduced by the calculation of the time-sample by time-sample median waveform value over all emissions after the rejection of the outliers. This median waveform, however, was not considered to be the most appropriate representation of the airgun's acoustical output because the sample-wise median process made unphysical discontinuities between samples a possibility. Instead, the single-emission waveform, which lay closest to the median waveform, was used because this captured the airgun's output from a single, representative emission. This process for handling repeatability across measurements is proposed as a reasonable approach, but alternative methods might be used and investigations of the consequences of such methods would represent an interesting and useful study.

The finite repeatability of the source waveforms over the emissions stems from multiple causes. Whereas airgun emissions at low frequencies are remarkably consistent, stochastic physical processes are significant at higher frequencies (MacGillivray, 2019). This leads to an intrinsic
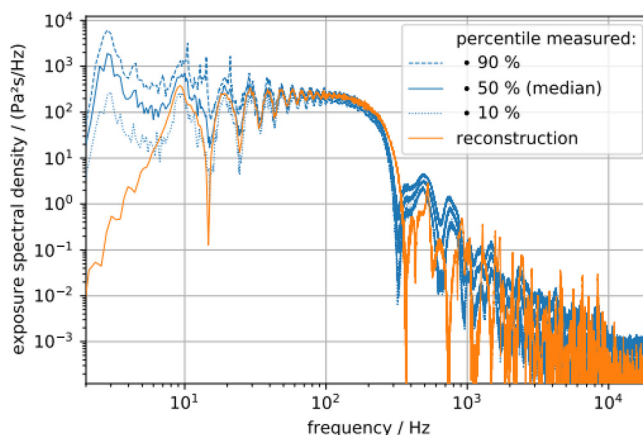

FIG. 15. (Color online) The spectra of the pressure at a deep hydrophone measured (blue lines) and predicted by the reconstruction (orange line) for a G-gun of volume 400 in.[3] (6.55 L), operated at a chamber pressure of 2000 lbf/in.[2] (13.79 MPa) and deployed at a depth of 6 m.
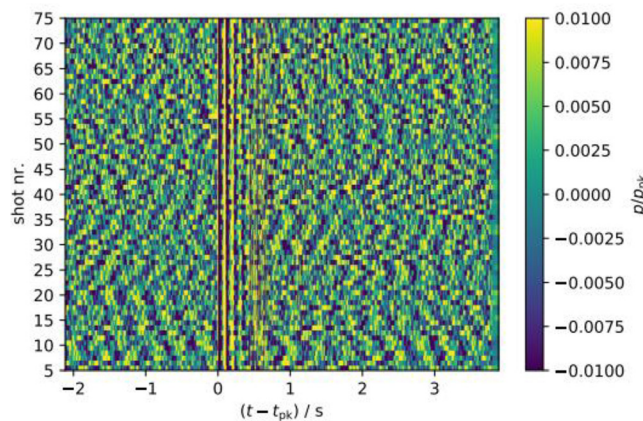

FIG. 17. (Color online) The shaded image representation of multiple time-series of the received pressure from a sequence of emissions for a Bolt gun of volume 150 in.[3] (2.46 L), operated at a chamber pressure of 1800 lbf/in.[2] (13.79 MPa) and deployed at a depth of 2 m.
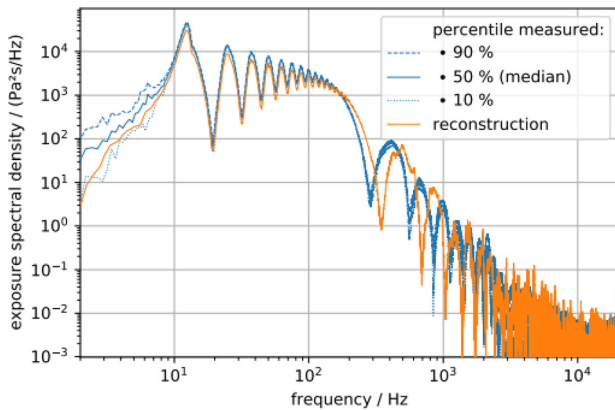
FIG. 18. (Color online) The spectra of the pressure at a deep hydrophone measured (blue lines) and predicted by the reconstruction (orange line) for a G-gun of volume 60 in.^{3} (0.98 L), operated at a chamber pressure of 2500 lbf/in.^{2} (13.79 MPa) and deployed at a depth of 3 m.

emission-to-emission variability in the source waveform. In addition, an airgun's acoustical output may change over a sequence as its temperature increases after initial emissions until it has reached a steady-state temperature at which point the heat generated during each discharge is dissipated between the successive emissions. The measurement geometry, which involved repeated emissions of a stationary airgun, also resulted in inter-emission changes in the concentration of air bubbles in the water around the gun. This concentration was not measured but is likely to have altered the acoustical output from the airguns resulting from modifications to the local seawater density and compressibility.

The finite repeatability across measurements and the subsequent spread in source waveforms and metrics represents a natural precision applicable to the assessment of any mismatch with the predicted waveforms produced by the airgun source models.

Whereas the SV dataset represents a characterization of the acoustic output of multiple airgun types and sizes, developments have been made in the field of airgun design since the dataset was gathered. In particular, increasing concern regarding the impact of airgun-generated sound on marine life has motivated efforts to produce airguns with reduced high-frequency emissions (Coste *et al.*, 2014). The source waveforms of such new devices are not included in this dataset, and it would be desirable for them to be included in future efforts at airgun characterization.

VIII. SUMMARY AND CONCLUSIONS

Measurements of the acoustic pressure recorded at hydrophones in the vicinity of the marine-seismic airguns were used to derive the characterizations of their acoustical output. Limited information related to the calibration of near-field hydrophones meant that a novel characterization method had to be developed to derive the source waveforms from the pressure measurements made on hydrophones outside the acoustical near-field.

The airguns' acoustical output was described in terms of the source waveform, which has dimensions of the pressure-times-distance and is sometimes referred to as the "notional signature." Further characterization was achieved via metrics such as the peak source waveform and energy source factor. These metrics were calculated for several frequency bands, including those most relevant to the seismic imaging and broader bands, including high-frequency sound that is important in the calculation of the impact of sound on marine life.

The validity of these characterizations was demonstrated via the regression fits based on the metrics describing the acoustical output in terms of the peak values and time-integrated squared-signature. These fits were shown to agree with similar fits from the open literature and predict metrics to within ∼2 dB. The source characterizations were further validated by comparison of the measured sound pressure at far-field hydrophones and predictions of sound pressure made using the source characterizations.

The validity of the source characterizations at the highest frequencies considered (>8 kHz) remains subject to considerable uncertainty because airguns transmit energy at these frequencies for only a small proportion of their signals' total duration. Consequently, metrics such as the energy source level, which are integrated over the entire duration of the pulse, are affected significantly by the background noise. The measures required to redress this problem are worthy of further study.

Ainslie, M. A., De Jong, C. A. F., Halvorsen, M. B., and Ketten, D. R. (**2018a**). "Underwater acoustics—Task 1: Terminology. A report prepared by TNO for the Joint Industry Programme on E and P Sound and Marine Life," JIP Topic—Sound Source Characterisation and Propagation, TNO, Den Haag, Netherlands.

Ainslie, M. A., Halvorsen, M. B., Dekeling, R. P., Laws, R. M., Duncan, A. J., Frankel, A. S., Heaney, K. D., Küsel, E. T., MacGillivray, A. O., Prior, M. K., Sertlek, H. Ö., and Zeddies, D. G. (**2016**). "Verification of airgun sound field models for environmental impact assessment," Proc. Mtgs. Acoust. **27**, 070018.

Ainslie, M. A., Hartstra, I., MacGillivray, A., Laws, R. M., Halvorsen, M. B., Müller, R., Wang, L., and Prior, M. K. (**2020**). "Report on task 2 of project 'SVOW OGP JIP airgun measurements': Characterise sources," TNO, Den Haag, Netherlands.

Ainslie, M. A., Heaney, K. D., and MacGillivray, A. O. (**2019**). "Guest editorial special issue on verification and validation of air gun source signature and sound propagation models," IEEE J. Ocean. Eng. **44**, 551–559.

Ainslie, M. A., Miksis-Olds, J., Martin, B., Heaney, K., de Jong, C., von Benda-Beckmann, A. M., and Lyons, A. (**2018b**). "ADEON underwater soundscape and modeling metadata standard," version 1.0, Technical Report by JASCO Applied Sciences for ADEON Prime Contract No. M16PC00003.

Barry, K. M., Cavers, D. A., and Kneale, C. W. (**1975**). "Recommended standards for digital tape formats," Geophysics **40**, 344–352.

Coste, E., Gerez, D., Groenaas, H., Larsen, O. P., Wolfstirn, M., Hopperstad, J.-F., Laws, R., Norton, J., Padula, M., and Wolfstirn, M. (**2014**). "Attenuated high-frequency emission from a new design of airgun," in *SEG Technical Program Expanded Abstracts 2014*, Society of Exploration Geophysicists, pp. 132–137.

Dekeling, R. P., Tasker, M. L., Van der Graaf, A. J., Ainslie, M. A., Andersson, M. H., André, M., Dekeling, R. P. A., Tasker, M. L., Van der

J. Acoust. Soc. Am. **150** (5), November 2021

Prior *et al.* 3691

Graaf, A. J., Ainslie, M. A., Andersson, M. H., André, M., Borsani, J. F., Brensing, K., Castellote, M., Cronin, D., Dalen, J., Folegot, T., Leaper, R., Pajala, J., Redman, P., Robinson, S. P., Sigray, P., Sutton, G., Thomsen, F., Werner, S., Wittekind, D., and Young, J. V. (**2014**). "Monitoring guidance for underwater noise in European seas, Part II: Monitoring guidance specifications," Marine Strategy Framework Directive Technical Subgroup on Underwater Noise, Publications Office of the European Union, Luxembourg; available at https://prod.repository.oceanbestpractices.org/handle/11329/1237.

Dragoset, B. (**2000**). "Introduction to air guns and air-gun arrays," Leading Edge **19**, 892–897.

Duncan, A. J., and Gavrilov, A. N. (**2019**). "The CMST Airgun Array Model—A simple approach to modeling the underwater sound output from seismic airgun arrays," IEEE J. Ocean. Eng. **44**, 589–597.

Duncan, A. J., Weilgart, L. S., Leaper, R., Jasny, M., and Livermore, S. (**2017**). "A modelling comparison between received sound levels produced by a marine Vibroseis array and those from an airgun array for some typical seismic survey scenarios," Mar. Pollut. Bull. **119**, 277–288.

Ewing, J., and Zaunere, R. (**1964**). "Seismic profiling with a pneumatic sound source," J. Geophysical Research **69**(22), 4913–4915.

Fields, D. M., Handegard, N. O., Dalen, J., Eichner, C., Malde, K., Karlsen, Ø., Skiftesvik, A. B., Durif, C. M. F., and Browman, H. I. (**2019**). "Airgun blasts used in marine seismic surveys have limited effects on mortality, and no sublethal effects on behaviour or gene expression, in the copepod *Calanus finmarchicus*," ICES J. Mar. Sci. **76**, 2033–2044.

Giles, B. F., and Johnston, R. C. (**1973**). "System approach to air-gun array design," Geophysical Prospecting **21**(1), 77–101.

Goertz, A., Wisløff, J. F., Drossaert, F., and Ali, J. (**2013**). "Environmental source modelling to mitigate impact on marine life," First Break **31**, 59–64.

Heaney, K. D., and Campbell, R. L. (**2016**). "Parabolic equation modeling of a seismic airgun array," IEEE J. Oceanic Engineering **44**(3), 621–632.

IAGC, O. G. (**2011**). "An overview marine seismic operations," International Association of Oil and Gas Producers, Report 448.

IEC-International Electrotechnical Commission. (**2016**). IEC 61260-3, Geneva, Switzerland.

ISO (**2017**). 18405, "Underwater acoustics—Terminology" (International Organization for Standardization, Geneva, Switzerland).

Jensen, F. B., Kuperman, W. A., Porter, M. B., Schmidt, H., and Tolstoy, A. (**2011**). *Computational Ocean Acoustics* (Springer, New York), Vol. 2011.

Johnston, R. C., Reed, D. H., and Desler, J. F. (**1988**). "SEG standards for specifying marine seismic energy sources," Geophysics **53**(4), 566–575.

Laws, R. M., Hatton, L., and Haartsen, M. (**1990**). "Computer modelling of clustured airguns," First Break **8**, 331–344.

Laws, R., Landrø, M., and Amundsen, L. (**1998**). "An experimental comparison of three direct methods of marine source signature estimation," Geophys. Prospect. **46**, 353–389.

Lundsten, T. (**2010**). *JIP Recording Overview*, 7th ed. (Petroleum Geo-Services ASA, Lilleaker, Norway).

MacGillivray, A. O. (**2006**). "Acoustic modelling study of seismic airgun noise in Queen Charlotte Basin," Ph.D. dissertation, University of Victoria, B.C., Canada.

MacGillivray, A. O. (**2019**). "An airgun array source model accounting for high-frequency sound emissions during firing—Solutions to the IAMW source test cases," IEEE J. Ocean. Eng. **44**, 582–588.

Mattsson, A., Parkes, G., and Hedgeland, D. (**2012**). "Svein Vaage broadband air gun study," in *The Effects of Noise on Aquatic Life* (Springer, New York), Vol. 730, pp. 469–471.

McCauley, R. D., Day, R. D., Swadling, K. M., Fitzgibbon, Q. P., Watson, R. A., and Semmens, J. M. (**2017**). "Widely used marine seismic survey air gun operations negatively impact zooplankton," Nat. Ecol. Evol. **1**, 0195.

NMFS. (**2018**). "2018 revisions to: Technical guidance for assessing the effects of anthropogenic sound on marine mammal hearing (version 2.0): Underwater thresholds for onset of permanent and temporary threshold shifts," (NMFS, USA); available at https://repository.library.noaa.gov.

NOAA, N. O. (**2016**). "Technical guidance for assessing the effects of anthropogenic sound on marine mammal hearing underwater acoustic thresholds for onset of permanent and temporary threshold shifts," NOAA Technical Memorandum, (NOAA, USA); available at https://repository.library.noaa.gov/.

Pramik, B. (**2013**). "Marine Vibroseis: Shaking up the industry," First Break **31**, 67–72.

Prior, M. R. (**2018**). "Report on Task 1B of Project 'SVOW OGP JIP Airgun Measurements': Characterising sound pressure measurements," TNO, Den Haag, Netherlands.

Prior, Mark K., Müller, R., Hartstra, I., Ainslie, M. A., MacGillivray, A., Halvorsen, M., Wang, L., Robinson, S., and Laws, R. (**2018**). "Report on Task 1B of project "SVOW OGP JIP airgun measurements": Characterising Sound Pressure measurements". TNO Report R11079.

Prior, M. K., Duncan, A. J., Sertlek, H. Ö., and Ainslie, M. A. (**2019**). "Modeling acoustical pressure and particle acceleration close to marine seismic airguns and airgun arrays," IEEE Journal of Oceanic Engineering **44**(3), 611–620.

Sertlek, H. Ö., and Ainslie, M. A. (**2015**). "Airgun source model (AGORA): Its application for seismic surveys sound maps in the Dutch North Sea," in *Proceedings of Underwater Acoustic Conference and Exhibition 2015*, Crete, Greece, pp. 439–446.

Slabbekoorn, H., Dalen, J., de Haan, D., Winter, H. V., Radford, C., Ainslie, M. A., Heaney, K. D., van Kooten, T., Thomas, L., and Harwood, J. (**2019**). "Population-level consequences of seismic surveys on fishes: An interdisciplinary challenge," Fish Fisher. **20**, 653–685.

Southall, B. L., Bowles, A. E., Ellison, W. T., Finneran, J. J., Gentry, R. L., Greene, C. R., Jr., Kastak, D., Ketten, D. R., Miller, J. H., Nachtigall, P. E., Richardson, W. J., Thomas, J. A., and Tyack, P. L. (**2007**). "Marine mammal noise exposure criteria: Initial scientific recommendations," Aquatic Mammals **33**(4), 441–509.

Southall, B. L., Finneran, J. J., Reichmuth, C., Nachtigall, P. E., Ketten, D. R., Bowles, A. E., Ellison, W. T., Nowacek, D. P., and Tyack, P. L. (**2019**). "Marine mammal noise exposure criteria: Updated scientific recommendations for residual hearing effects," Aquat. Mammals **45**, 125–232.

Stone, C. J., and Tasker, M. L. (**2006**). "The effects of seismic airguns on cetaceans in UK waters," J. Cetacean Res. Manage. **8**, 255.

Vaage, S., Haugland, K., and Utheim, T. (**1983**). "Signatures from single airguns," Geophys. Prospect. **31**, 87–97.

Vaage, S., and Ursin, B. (**1987**). "Computation of signatures of linear airgun arrays," Geophysical prospecting **35**(3), 281–287.

Warner, G., MacGillivray, A. O., and Martin, S. B. (**2018**). "Analysis of acoustic particle motion data from the Svein Vaage airgun study," JASCO Applied Sciences, Environmental Studies Research Fund, Report 216, available at https://www.esrfunds.org/sites/www.esrfunds.org/files/publications/ESRF216_Warner,%20G_A_%20et%20al.pdf (Last viewed 10/22/2021).

Ziolkowski, A., Parkes, G., Hatton, L., and Haugland, T. (**1982**). "The signature of an air gun array: Computation from near-field measurements including interactions," Geophysics **47**, 1413–1421.